Structure and phases of the Au(001) surface: In-plane structure

Doon Gibbs and B. M. Ocko
Physics Department, Brookhaven National Laboratory, Upton, New York 11973

D. M. Zehner
Solid State Division, Oak Ridge National Laboratory, Oak Ridge, Tennessee 37831-6024

S. G. J. Mochrie
Physics Department and Center for Materials Science and Engineering, Massachusetts Institute of Technology, Cambridge, Massachusetts 02139
(Received 6 December 1989; revised manuscript received 14 May 1990)

We present the results of an x-ray-scattering study of the structure and phases of the clean Au(001) surface between room temperature and the bulk melting temperature of 1337 K. These experiments were performed in the glancing-incidence geometry, using an ultrahigh-vacuum apparatus for x-ray surface scattering. Three distinct surface structural phases have been identified. In the high-temperature phase ($1170 < T < 1337$ K), the x-ray-diffraction pattern has the (1×1) symmetry of the bulk, consistent with a disordered surface layer. At about $T = 1170$ K there is a reversible phase transition to an incommensurate, distorted-hexagonal structure. Below $T = 970$ K the surface has a rotated, distorted-hexagonal structure in which both the incommensurability and the average rotation angle are weakly temperature dependent. In this phase the line shapes of the hexagonal diffraction peaks show hysteresis, and the length scale over which there exists in-plane order is reduced.

I. INTRODUCTION

In this and a subsequent paper[1] we present the results of an x-ray-scattering study of the structure and phases of the clean Au(001) surface. Although this surface has been investigated extensively by modern surface-science techniques, there still remain important, basic questions concerning its room-temperature structure. Considerably less is known about the structure at higher temperatures—for example, near the bulk melting temperature of $T = 1337$ K. Like the (001) faces of Pt and Ir, the Au(001) surface layer is believed to be hexagonal at room temperature, in contrast to the square symmetry of the bulk lattice planes lying immediately beneath.[2] It has further been suggested that the hexagonal lattice is incommensurate with respect to the bulk, and that the surface supports rotated domains.[2–11] Yet, a definitive determination of either the incommensurability or the rotation angle has remained elusive. More recently, on the basis of absolute measurements of the specular reflectivity, we have speculated that the top layer of the Au(001) surface layer may melt about 150 K below the bulk melting temperature.[11] A detailed understanding of this behavior, including orientational epitaxy, commensurate-incommensurate reconstructions, and two-dimensional melting, in elemental metal surfaces is of fundamental importance to the study of two-dimensional structures and phase transitions. These issues have stimulated a vast effort in the study of rare-gas adsorbates on graphite surfaces.[12–14] In addition, high-temperature studies are the essential ingredient in an understanding of the global stability of crystal surfaces and of the relationship between such phenomena as roughening transitions, enhanced surface vibrations, and surface and bulk melting. Synchrotron-based x-ray-scattering techniques bring special advantages to surface-structural studies, including straightforward interpretation of the measured intensities in terms of a three-dimensional (macroscopic) density distribution and naturally-high-wave-vector transfer resolution. As a result, the pace of x-ray studies of metal surfaces has quickened during the last two years, with experiments having now been performed on the (110) faces of Au,[15] Ag,[16] Pb,[17] Pt,[18] and Cu,[19,20] the (001) faces of Au (Refs. 1 and 11) and W,[21] and on the (111) faces of Pb (Ref. 17) and Au.[22] X-ray experiments on semiconductor surfaces and on metals adsorbed on semiconductors are reviewed in Ref. 23.

In the present paper, we discuss the results of glancing-incidence x-ray-diffraction studies of the Au(001) surface. In the glancing-incidence geometry, the incident and exit x-ray angles typically fall within a degree of the critical angle for total external reflection ($\alpha_c = 0.63°$ for Au at a wavelength of $\lambda = 1.7$ Å). Owing to the small x-ray penetration depth, bulk contributions to the background are small, making this geometry convenient for quantitative investigations of in-plane surface structure. In a future paper,[1] we plan to discuss the results of specular and nonspecular reflectivity studies of the Au(001) surface. There the incident and exit angles may increase to 45°, or larger. As will become apparent, this geometry is useful for characterizing the structure of the top and succeeding layers along the direction of the surface normal. A full description of both geometries is contained within the three-dimensional x-ray cross sec-

tion (which is specialized to solid surfaces in Ref. 1, and both are crucial to investigations of surface structure.

Briefly, we have identified three distinct structural phases exhibited by the Au(001) surface between $T=300$ K and the bulk melting transition at $T=1337$ K. They are (1) disordered ($1170<T<1320$ K), (2) distorted-hexagonal ($970<T<1170$ K), and (3) rotated, distorted-hexagonal ($300<T<970$ K). The symmetries of the diffraction patterns for these phases are shown in Fig. 1, where the data obtained in the glancing-incidence geometry are summarized. In the figure, each symbol represents a rod of scattering extending normal to the (001) planes. The rod scattering through the origin of reciprocal space is the specular reflectivity, while the off-axis rod scattering is the nonspecular reflectivity.

The diffraction pattern observed in the high-temperature phase between $T=1170$ and 1337 K is shown in Fig. 1(a). Solid squares are indexed in bulk-cubic reciprocal-lattice units $(H,K,L)c$ and represent the reflectivity along directions normal to the surface joining all the bulk Bragg reflections. In the literature, these rods are referred to as crystal-truncation rods.[24] Thus, the area enclosed by the solid squares corresponds to the substrate unit cell. At elevated temperatures, the diffraction pattern has the (1×1) symmetry of the bulk, consistent with an unreconstructed or disordered surface layer. This phase will be discussed extensively in Ref. 1.

Below $T=1170$ K, there is a reversible transition to an incommensurate, two-dimensional structure of hexagonal symmetry. Hexagonal reciprocal-lattice vectors $(1,0)h$ and $(0,1)h$ are indicated by open triangles in Fig. 1(b). Surrounding each are additional satellites along directions parallel to the bulk [110] direction. These are indicated by solid circles in Fig. 1. The separation between harmonics is the incommensurability $\delta=0.206(\pm0.001)$ $\sqrt{2}c^*$ ($c^*=2\pi/c=3.081$ Å^{-1} at room temperature). As shown below, these satellites arise from modulations of the surface layer by the underlying square lattice (and vice versa), and may be indexed as sums and differences of surface and bulk wave vectors. We call this phase the distorted-hexagonal phase.

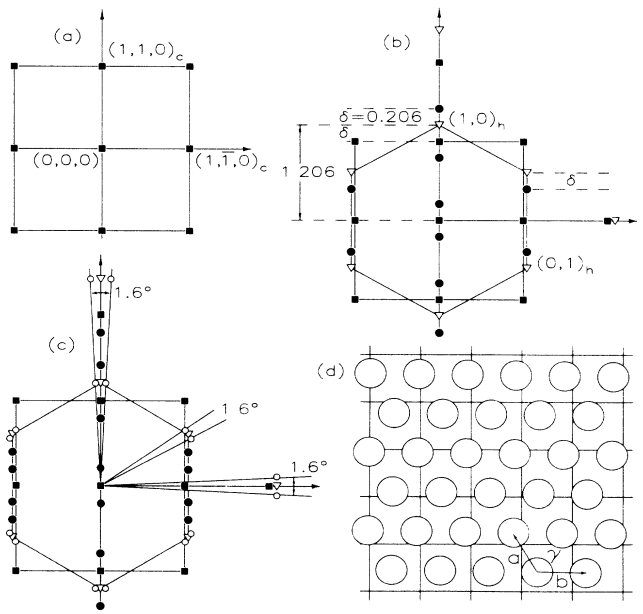

FIG. 1. In-plane diffraction pattern $(H, K, 0.07)c$ for (001) surface of Au. (a) Disordered phase, (b) distorted-hexagonal phase, and (c) rotated, distorted-hexagonal phase. Each point represents a rod of scattering extending normal to the surface. Bulk $[110]c$ and $[1\bar{1}0]c$ directions are indicated. Peaks corresponding to domains rotated by 90° were observed, but are not shown. All the data represented in Fig. 1 were obtained at fixed $L=0.07$ in bulk reciprocal-lattice units. (d) Real-space schematic view of a rotated domain.

Below $T=970$ K, additional rods appear around each of the hexagonal rods, as shown by the open circles in Fig. 1(c). These occur at a fixed angle equal to $\pm0.81°$ away from the [110] direction, and reveal the existence of rotated domains (in coexistence with the aligned domains). In addition, higher harmonics are visible along the [110] direction [solids circles, Fig. 1(c)]. The transition to the rotated, distorted-hexagonal phase is reversible. It is surprising, when compared to the behavior of rare-gas adsorbates on graphite,[12–14] that the rotation angle and the incommensurability are observed to be only weakly temperature dependent between $T=1170$ and 300 K. Nevertheless, important features of the line shapes below $T=970$ K depend sensitively on temperature and on sample history. For example, the correlation lengths are resolution-limited (>1000 Å) in the distorted-hexagonal phase, but decrease continuously as the temperature is lowered below $T=970$ K. Further, the transverse line shapes below $T=970$ K clearly display hysteresis for increasing and decreasing temperatures, and for different cooling rates. The observation of hysteresis raises important questions about the possibility of attaining true thermodynamic equilibrium in the rotated, distorted-hexagonal phase.

It is important to add that by modeling the observed reflectivity along the hexagonal rods and their satellites (the data and analysis are presented in Ref. 1), we have found that the interplaner spacing between the top and second layers is expanded by 19% relative to the bulk spacing, in agreement with earlier work.[11] Furthermore, it is found that the top layer is corrugated with a peak-to-peak amplitude of 28% relative to the interlayer spacing along the surface normal, and that this buckling propagates to the second and succeeding layers (with diminished amplitude). In the model of the surface discussed in the following paper,[1] it is shown that the corrugation wave vector equals the incommensurability. Despite the buckling and expansion, the net volume density of the reconstructed Au(001) surface selvedge is, nevertheless, slightly increased relative to an ideally terminated bulk, due to the higher packing density within the hexagonal layers. A summary of the present results and those of Ref. 1 has been given in Ref. 25.

Before turning to the present x-ray experiments, we summarize some related features of earlier work on the Au(001) surface obtained by other techniques at room temperature. Analysis of the diffraction pattern obtained by low-energy electron diffraction (LEED) is consistent

with a large unit cell, approximately (1×5), of hexagonal symmetry.[2–7] A precise determination of the incommensurability has remained outside the resolution of the LEED experiments attempted so far. The additional 25% mass required for such a layer has been directly detected by ion scattering.[4] Scanning-tunneling-microscopy measurements[7] have also reported a hexagonal unit cell, possibly incommensurate, but contracted relative to bulk (111) planes by 4.4% along the [110] direction and by 3.8% along the $[1\bar{1}0]$ direction. Rotated domains were reported with a rotation angle of about 0.1°. More recent transmission-electron-microscopy (TEM) and transmission-electron-diffraction (TED) measurements[10] also report a hexagonal unit cell, contracted by 3.6% in the [110] direction and by 3.3% in the $[1\bar{1}0]$ direction. Top-layer rotation angles as large as $\pm0.7°$ were inferred. In the latter experiments, the authors emphasize the importance of local variations of the structure, depending, for example, on the step distribution across the surface. As will become clear, our results for the symmetry and dimensions of the room-temperature unit cell, the rotation angle, and the incommensurability extend those summarized here. In our view, the differences between our results and those of earlier studies arise, in part, from the high accuracy possible in structural determinations by x-ray-scattering techniques, and also from variations of the sample quality and preparation conditions used by different groups.

II. SURFACE APPARATUS AND PREPARATION

For the results reported here and in Ref. 1, two different surface chambers were employed. A small, portable high-vacuum chamber was used to collect data at large incidence angles at Beamline A2 at the Cornell High Energy Synchrotron Source (CHESS) and at X20C and X22B at the National Synchrotron Light Source (NSLS) at Brookhaven National Laboratory. A detailed description and discussion of these results is given in Ref. 1. The in-plane measurements reported in this paper were performed on Beamline X22C at the NSLS using a versatile, ultrahigh-vacuum (UHV) apparatus for surface x-ray scattering. The assembled results from measurements of two different samples and in both vacuum chambers agree in detail. Beamline X22C utilizes a double-focusing nickel-coated mirror (spot size less than 1 mm^2) and a two-crystal vertical diffraction Ge(111) monochromator. The x-ray wavelength for these experiments was $\lambda=1.710$ Å. A detailed description of the beamline is given elsewhere.[26] Because the UHV apparatus is new, we describe its basic features in more detail.

A schematic view of the apparatus is shown in Fig. 2. The main features include a vertical diffraction six-circle spectrometer, a large 200° Be window electron-beam-welded directly to the scattering chamber, a differentially pumped rotary seal, and provision for such standard surface diagnostics as LEED, Auger-electron spectroscopy (AES), residual-gas analysis, and ion sputtering. The sample temperature can be varied between $T=300$ and 2000 K. After bakeout, the base pressure of the chamber falls to 1×10^{-10} Torr or less. The spectrometer is coupled to the sample through a differentially pumped rotary seal and a bellows, which permits the sample to be rotated through its Euler angles (θ,χ,ϕ) while residing in the vacuum. The spectrometer, fabricated by Franke-Heydrich, Inc.,[27] was designed for very-high-resolution experiments. Individual rotary tables have absolute angular accuracy approaching 0.001°, with a measured repeatability of about 0.0001°. The present design utilizes the concept of synchronously driven arcs for the χ rotation first implemented by Fuoss and Robinson,[28] but extends that idea by increasing the available angle to $\pm20°$, by introducing an additional rotation of the apparatus around the vertical axis, and by fixing the sample within the scattering chamber. The fixed sample geometry complicates the design of the vacuum chamber, but leads to straightforward sample alignment and heating. Furthermore, it permits both x-ray diffraction and *in situ* sample characterization. Finally, the introduction of a sliding table for the vacuum chamber simplifies sample access, and permits use of the spectrometer for other types of diffraction experiments. Fabrication of the vacuum chamber and electron-beam welding of the Be window were performed by Electrofusion, Inc.[29]

The 2-mm-thick–by–10-mm-diam sample was cut from the same ingot as the sample studied in earlier reflectivity measurements.[11] As noted in Ref. 1, specular-reflectivity studies of this sample reproduced the results obtained with the first sample. The crystal, oriented to $<0.25°$ of [001], was mounted on a Ta disk which itself was supported by a (potted) button heater. The sample temperature was monitored by means of a Chromel-Alumel thermocouple, by a pyrometer, and by measurement of the gold lattice constant. After mechanical and electrochemical polishing the mosaic full width at half maximum (FWHM) at the bulk (002) reflection was found to be $>1°$. During extended sputtering and annealing cycles at elevated temperatures (near the bulk melting temperature), the mosaic widths of the (131) and symmetry-equivalent reflections were observed to decrease to $<0.01°$. Clean surfaces, as determined from AES spectra obtained using a single-pass cylindrical mirror analyzer (CMA), were prepared by Ar^+-ion bombardment (1 kV and 7 μA), followed by a high-temperature anneal. This procedure always yielded stable, reproducible diffraction patterns for extended periods.

A separate UHV system equipped with four-grid LEED optics, a double-pass CMA, and an ion gun was used for the purpose of sample characterization. After preparation, the sample was inserted in this chamber, cleaned, and characterized. Measurements were obtained over the same sample temperature range as that used in the x-ray studies. In order to assess the effects on the sample of extended heating at temperatures near the melting point, it was again characterized in this chamber subsequent to the x-ray studies.

A clean surface from which no impurities could be detected within the sensitivity limits of AES ($\sim1\%$ of a monolayer) was easily obtained by sputtering and annealing to ~600 K. The LEED pattern obtained showed the surface to be reconstructed.[2] However, in the initial stages of sample preparation, small amounts of Ca were

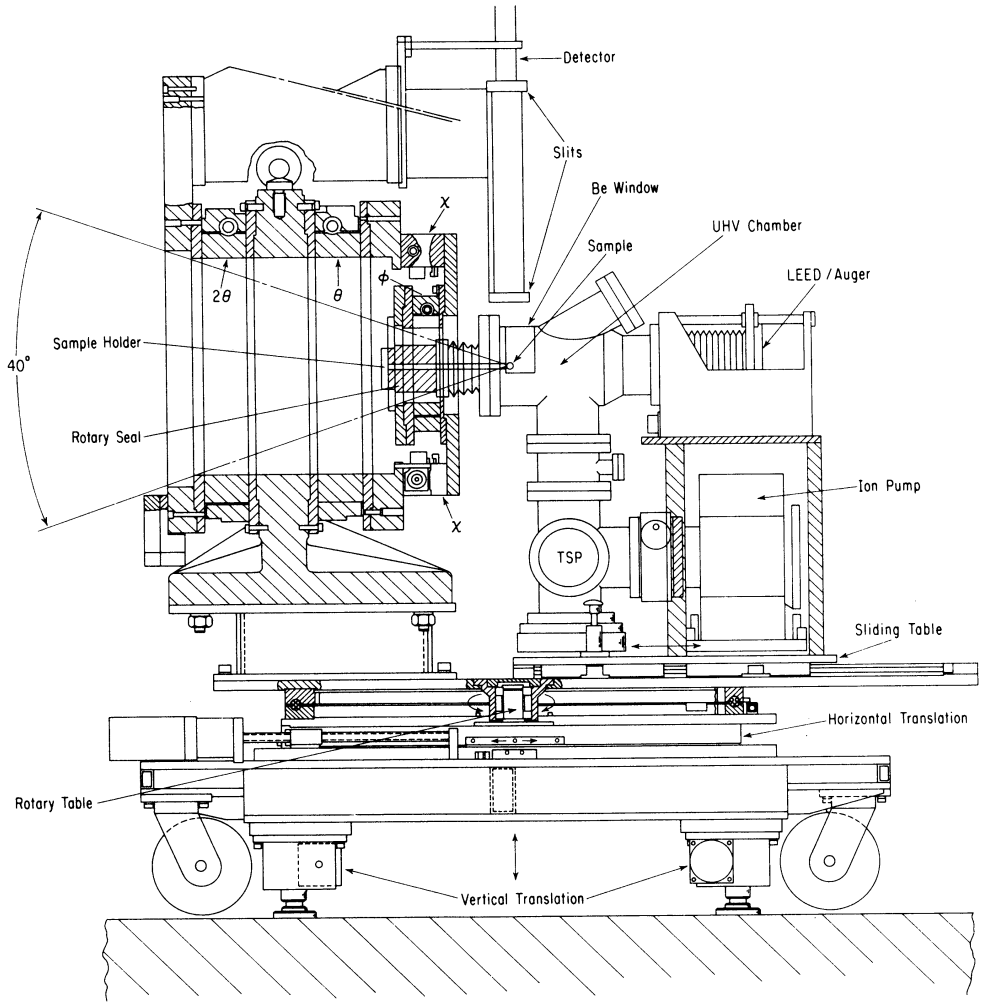

FIG. 2. UHV surface x-ray-scattering apparatus implemented on NSLS beamline X22C. Incident-beam direction is into the paper through the Be window and onto the sample.

observed on the surface following high-temperature annealing (>1100 K). Similar observations have been reported in earlier LEED studies of Au surfaces.[4] After extended sputtering and annealing cycles at temperatures >1100 K, Auger-electron spectra indicated Ca concentrations of $<1\%$, when it was detectable. The presence of Ca at these concentrations had no effect on the observed LEED patterns. Scanning-electron-microscopy and electron-induced x-ray-fluorescence measurements performed subsequent to the x-ray experiments confirmed the existence of small (~ 1-μm) localized Ca deposits. These are presumably located at grain boundaries, and occur in areal concentrations of less than 1%. (The bulk Ca concentration was determined to be 2 ppm.) Because the Ca is confined to localized deposits, the actual Ca coverage of the surfaces we studied must be much less than this. No other impurities were detected. To within the sensitivity of our diagnostics, the possible presence of Ca during our experiments had no effect on the results reported here.

The in-plane experiments were performed near-glancing incidence in a vertical diffraction-reflection geometry. The incident and exit x-ray angles α and β were always chosen to be equal, and to preserve the surface normal index $L=0.07$. This value of L corresponds to an incident angle $\alpha > \alpha_c$ and was used because it gave maximum intensity at the surface peaks. Except for the scans shown in Figs. 3, 16, and 17, all of the data reported here were obtained using a Ge(111) analyzing crystal placed after the sample. These scans are referred to in the text as high-resolution scans. Low-resolution scans were performed upon removal of the analyzing crystal. The resolution is then determined by the slit settings on the 2θ arm. The slits on the 2θ arm before the detector were left open in the horizontal (2 cm separation) and in the vertical (4 mm separation) directions so that all of the x rays scattered at a given 2θ were collected. (The distance between the sample and the slits was 0.7 m.) A detailed discussion of the three-dimensional x-ray cross section specialized to this geometry, including the resolution function, is given in Ref. 1.

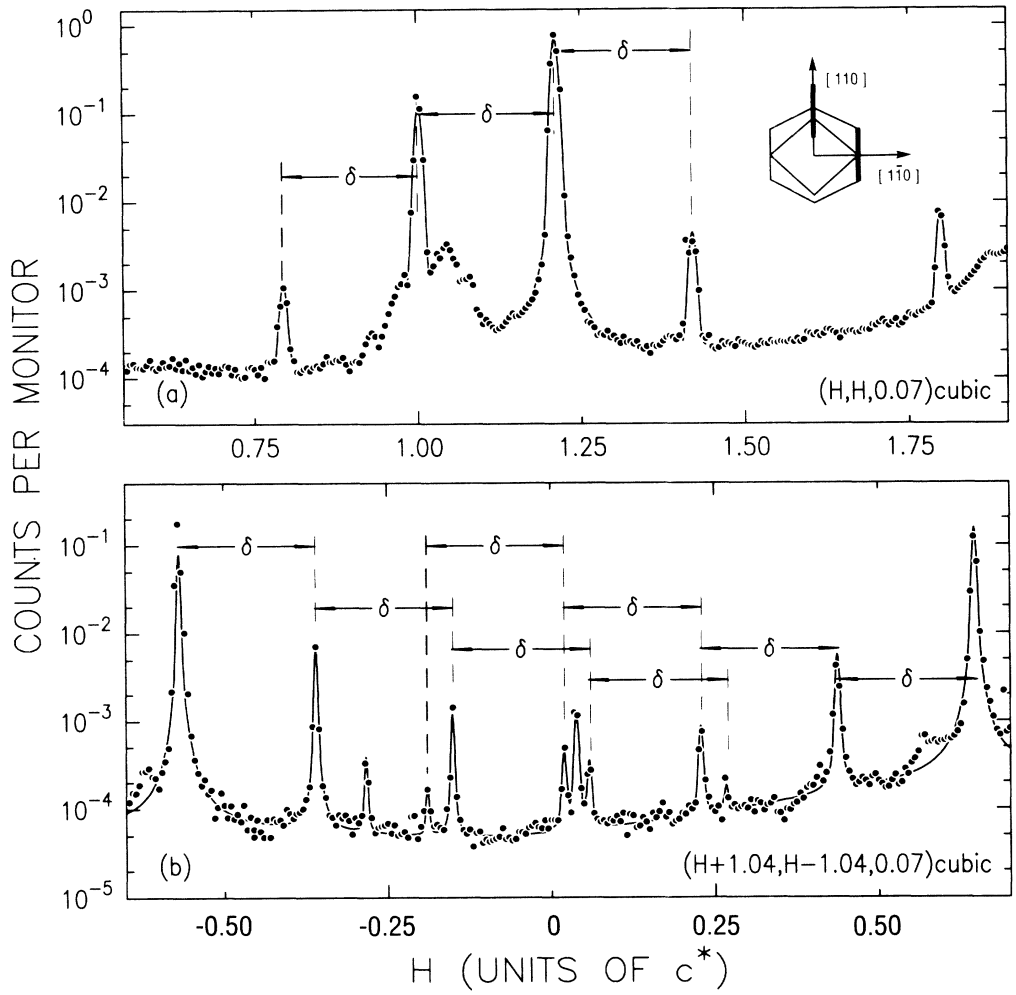

FIG. 3. Upper: scan through $(1, 1, 0.7)c$ and $(1,0)h$. Lower: scan through $(0,1)h$ and $(1,1)h$. Inset: the paths traversed through reciprocal space in each case. The index is H in cubic reciprocal-lattice units. Solid lines are the results of fits to the data.

III. RESULTS AND DISCUSSION

A. Distorted-hexagonal unit cell

Figure 3 shows the results of two typical low-resolution scans through the putative hexagonal reciprocal lattice at room temperature, plotted on a logarithmic scale. The data were obtained after sputtering and then annealing the sample to $T=1000$ K for 24 h. The paths traversed through reciprocal space are shown inset in the top panel. The index H in the figure is the first component of $(H,K,L)c$, expressed in bulk-cubic units. Because the substrate has square symmetry, the surface has two equivalent domains related by a 90° rotation of the sample about the cubic [001] direction. In the experiments reported here, both domains yielded identical results, and therefore only one was examined in detail.

Shown in the top panel of Fig. 3 is the result of a scan from the origin in-plane through the $(1, 1, 0.07)c$ substrate peak, and beyond. The strongest peaks visible are the principal hexagonal peak at $(1,0)h=(H,K,L)c$ $=(1.206, 1.206, 0.07)c$ and the substrate peak at $(1, 1, 0.07)c$ (see Fig. 1). From this (and later high-resolution measurements) we conclude that, to within our resolution, the overlayer is weakly incommensurate with respect to the bulk. The magnitude of the difference between these two is the incommensurability $\delta=0.206\pm0.001\sqrt{2}c^*$ along the bulk [110] direction. It is worth remarking that all of the intensity at the hexagonal peaks arises from the surface reconstruction. In contrast, contributions to the scattering at substrate peaks arise from layers lying within about one penetration depth—several hundred angstroms for these incident and exit angles. Typical count rates for the principal hexagonal peak, absent the analyzing crystal, were about 10 000 per second on a background of <1 per second. The radial FWHM of the principal hexagonal peak determined using an analyzing crystal was about $(2\times10^{-3})c^*$, which corresponds to an in-plane correlation length $(=\pi/\text{FWHM})$ of about 1000 Å. This length is to be compared with the several-thousand-angstrom single-step dimension determined by reflectivity methods for this sample.[11] Evidently, the in-plane crystalline order extends over a domain of length comparable to, but smaller than, a typical step dimension at room temperature. Higher harmonics of the principal hexagonal peak, which

are separated from it by integer multiples of the incommensurability, δ, are visible at $H\ (=K)=0.794c^*$, $1.412c^*$, and $1.794c^*$. We do not understand the origin of the weak scattering around the substrate peak at $(1, 1, 0.07)c$. It reappeared, although considerably weaker, in subsequent scans.

In the lower panel of Fig. 3 is shown the result of a scan taken at $T=300$ K, joining the $(0,1)h$ hexagonal peak on the left to the $(1,1)h$ hexagonal peak on the right. Four harmonics of each, one separated from the next by the incommensurability, δ, are visible. The peak at the center of the scan, near $H=0$, is the tail of the substrate peak at $(1, -1, 0.07)c$ [see Fig. 1(c)]. It is manifest from the splitting of the higher harmonics in Fig. 3(b) that the overlayer is incommensurate with the substrate. Because it never reappeared in subsequent, otherwise identical scans, we believe that the peak at $H=-0.2$ is spurious. Comparable intensities and full widths were obtained at the $(1,1)h$ and $(0,1)h$ hexagonal peaks as were obtained at the $(1,0)h$.

In this way, all of the in-plane peaks we have observed (see Fig. 1) may be indexed as sums and differences of the hexagonal peaks at $(1,0)h$, $(0,1)h$, and the substrate peak at $(1, 1, 0.07)c$. Equivalently, the in-plane peaks may be indexed as sums and differences of the hexagonal peaks and the incommensurability, δ. It follows that the hexagonal surface layer is modulated by the substrate potential (and vice versa), which leads to mixing of the surface and bulk periodicities in the x-ray-diffraction pattern.

Before discussing the origin of these peaks in more detail, we note the mean lattice constants of the surface-layer unit cell. From high-resolution scans of the incommensurability of the $(1,0)h$, $(0,1)h$, and $(1,2)h$ reflections, we have determined the average lattice parameters of the hexagonal unit cell to be $a=2.763\pm0.002$ Å, $b=2.766\pm0.002$ Å, and $\gamma=120.03°\pm0.1°$ at room temperature. The corresponding quantities for bulk cubic (111) planes are $a=2.885$ Å, $b=2.885$ Å, and $\gamma=120°$. This implies that the overlayer is contracted by 4.3% in the [110] direction and by 4.2% in the $[1\bar{1}0]$ direction. The relative orientation of the hexagonal unit cell and the cubic unit cell is established by the collinearity of the $(1,0)h=(1.206, 1.206, 0.07)c$ and $(1, 1, 0.07)c$ reflections. It is important to note that with these average lattice constants the overlayer is hexagonal, to within the experimental error, and incommensurate with the square substrate in both directions along the surface.

The modulation of the surface by the underlying lattice may be pursued formally by considering the structure factor of a perturbed two-dimensional layer. In the weak-modulation limit, the displacements of atoms in the overlayer (ζ) are a simple sinusoidal function of position: $\zeta(\mathbf{r})=\zeta_0\sin(\mathbf{g}\cdot\mathbf{r})$, where $\mathbf{g}=(\delta,\delta,0)c$ is the modulation wave vector. In this case, one expects the intensity of the nth satellite to scale as $(\mathbf{Q}\cdot\zeta_0)^{2n}$.[30] It is evident from Fig. 3(b) that the satellite intensities decrease more slowly than this, indicating that there are higher harmonics in the displacement. Such behavior is expected for overlayers that are close to commensurability with the substrate. In this case, the hexagonal peak at $(1.206, 1.206, 0.07)c$ is close to the commensurate position at $(\frac{6}{5}, \frac{6}{5}, 0.07)c$. If the ratio were exactly $\frac{6}{5}$, then six oblique lattice units would match exactly with five squares of the bulk substrate—a fivefold commensurability. We note in this regard that despite the near match of the bulk substrate wave vector at $(2, -2, 0.07)c$ and the near-hexagonal wave vector at $(1,2)h$ [see Fig. 1(b)], we see no additional peaks associated with a modulation in the $[1\bar{1}0]$ direction.

Thus, we are led to a discommensuration model of the Au(001) surface, where locally commensurate regions (commensurate in only one direction) are separated by linear discommensurations running perpendicular to the [110] direction. To illustrate these ideas, we imagine that at each discommensuration the overlayer goes into registry with one of the $p=5$ possible commensurate sublattices. We further suppose that at each discommensuration the displacement is a fraction s/p of the commensurate unit cell, where s is an integer. Then, while the commensurate unit cell along the [110] direction is pa_s, the repeat distance is $D=Npa_s+sa_s$. Here, $a_s=2.885$ Å corresponds to the lattice constant of the square substrate and N is the number of commensurate unit cells between discommensurations. Diffraction peaks occur for every $Q=2\pi n/D$, where n is an integer. Referred to the nearest commensurate position, this may be rewritten

$$\frac{2\pi n}{(Np+s)a_s}=\frac{2\pi k}{pa_s}+\frac{2\pi}{D}(r-sk/p)\ ,$$

where $r=kN$ and k are integers. For the case of the Au(001) surface, $D=85.1$ Å. In the limit of narrow discommensurations, the structure factor for the unit cell may be explicitly calculated.[31,32] It turns out that the most intense peaks are those closest to the commensurate positions. The weak-modulation limit is recovered in this model when the width of a discommensuration approaches the separation between discommensurations. It seems likely that the structure of the Au(001) surface lies between these two limits (see, for example, Fig. 4). A more detailed understanding of the structure of the discommensurations will require crystallographic measurements of these and still more reflections. The first steps along these lines have been taken in Ref. 1, where it is shown that the displacement field is primarily a surface corrugation with a wave vector $\mathbf{g}$ equal to the incommensurability.

B. Rotated domains

Typical transverse scans (ω-rocking curves) across the hexagonal rods at $(1,0)h$, $(2,0)h$, and $(1,1)h$ and across the substrate rod at $(1, 1, 0.07)c$ are shown in Fig. 5, plotted on a logarithmic intensity scale, for $T=650$ K. In each of the scans through a hexagonal rod, there is a peak at the center with $\omega=0°$, and two adjacent peaks with $\omega=\pm0.81°\pm0.05°$. No additional peaks are observed in the scan through the substrate rod at $(1, 1, 0.07)c$. The solid lines in the figure show the results of fitting the data to Lorentzian line shapes, which proved superior to Gaussian line shapes for this analysis. While the fits clearly deviate in the wings, they are excel-

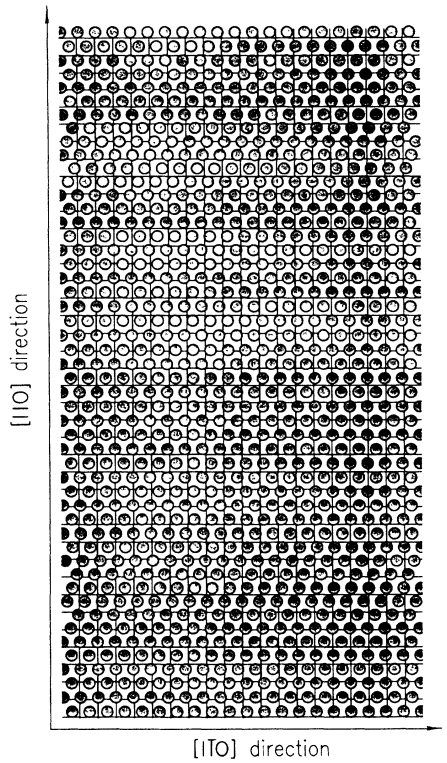

FIG. 4. Ball model of possible incommensurate domain walls running parallel to the [1$\bar{1}$0] direction, and separating locally commensurate regions. The $\hat{z}$-component of the displacement field (corrugation) is not shown.

lent in the neighborhood of the maxima, and give reliable values for the angular widths, peak positions, and peak intensities. When the data are plotted on a linear scale, the intensity is seen to be sharply peaked at $\omega=0°$, $\pm 0.81°$, and the deviations are not noticeable. In our view, still higher-resolution scans, taken over larger regions of reciprocal space, will be required before it can be determined whether the functional form of these line shapes is best described by a power law, as expected for an incommensurate, two-dimensional solid.

The absence of additional peaks around the substrate peak at $(1, 1, 0.07)c$ unambiguously identifies the peaks at $\omega=\pm 0.81°$ with the surface layer. The fact that the angular splitting is the same at $(2,0)h$ as it is at each corner of the hexagonal cell then establishes that the additional peaks arise from rotated, hexagonal domains [see Fig. 1(c)]. According to this interpretation, the rotation angle is just the value of ω. Because the three peaks have approximately equal intensities, we may infer that the populations across the surface of the unrotated and rotated hexagonal domains are sharply peaked at $\omega=0°$ and $\pm 0.81°$ and are roughly comparable in number at $T=650$ K. The rocking-curve widths (FWHM) for the unrotated peaks in Figs. 5(a), 5(b), and 5(c) are 0.18°, 0.16°, and 0.15°, respectively. The rocking-curve widths of the rotated peaks are 0.14°, 0.09°, and 0.09°, respectively. Thus, in each case the rotated peaks are narrower than the unrotated peak, but broader than the substrate peak at $(1, 1, 0.07)c$, whose width is 0.04°. All of these are

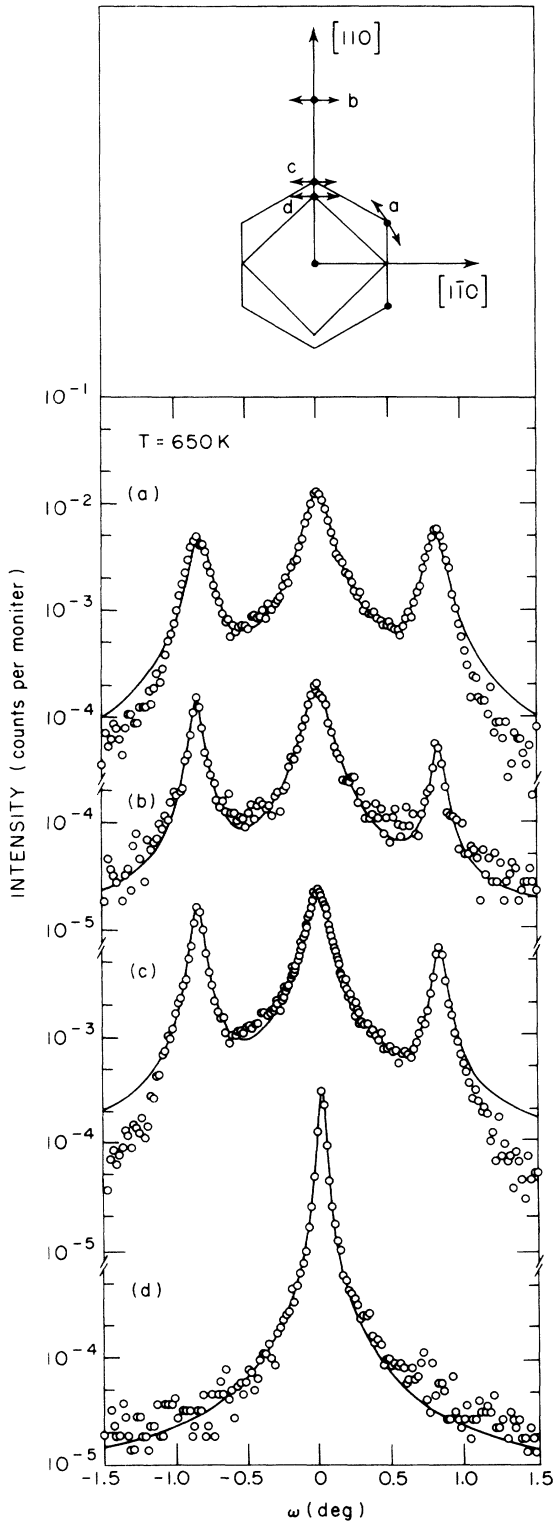

FIG. 5. Transverse scans through the surface $(1,0)h$, $(2,0)h$, $(1,1)h$, and bulk $(1, 1, 0.07)c$ peaks at $T=650$ K. The paths traversed through reciprocal space are indicated in the upper part of the figure. In (a)–(c), the peak at the center of the scan is the unrotated peak. The peaks split to the right and left are the rotated peaks. Solid lines are the results of Lorentzian fits.

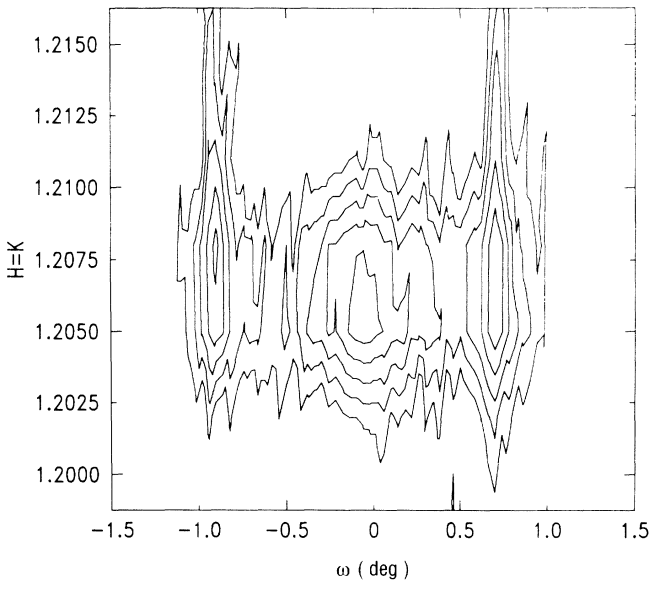

FIG. 6. Contour plot of the (1,0)h peaks at $T=840$ K, plotted on a logarithmic scale.

broader than the rocking-curve width of the bulk (1,3,1) reflection, which is $<0.01°$.

A two-dimensional view across the (1,0)h hexagonal rod and its rotated partners is given by the contour plot of Fig. 6 for $T=840$ K. The x-ray intensity is again plotted on a logarithmic scale in order to emphasize the behavior in the wings. The unrotated peak is clearly visible in the center with the rotated peaks split at $\pm 0.81°$ to either side. The longitudinal FWHM for the unrotated peak at this temperature is approximately $0.0017c^*$. In contrast, the longitudinal widths of the rotated peaks are about $0.003c^*$. Thus, the correlation length of the rotated domain is about half the correlation length of the unrotated domains at this temperature. Weak streaks of intensity are visible extending to higher momentum transfer for the rotated peaks, but not for the unrotated peak.

C. Temperature dependence

In this subsection, we discuss the temperature dependence of the diffraction pattern obtained for the Au(001) surface. The data presented here were accumulated from six different cycles of the temperature. Four of the cycles occurred for temperatures decreasing from about $T=1200$ K (that is, above the surface disordering transi-

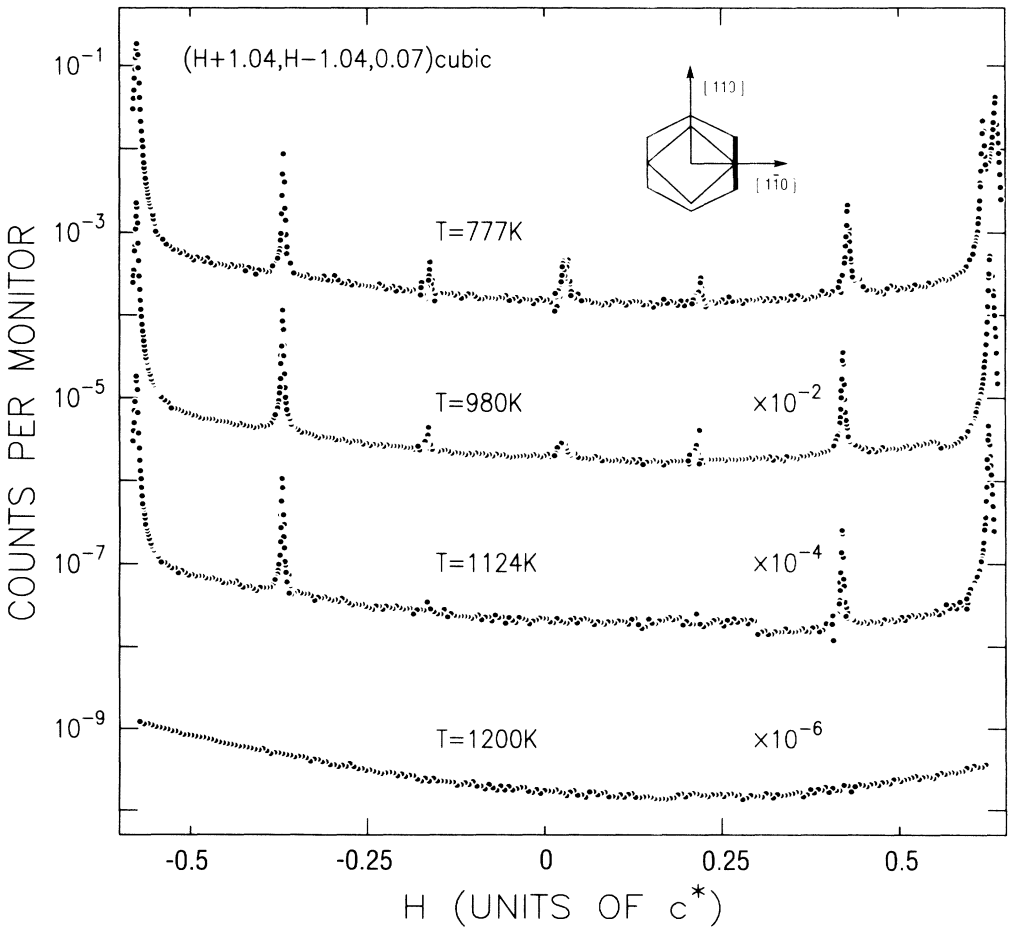

FIG. 7. Scans joining the near-hexagonal peak at (0,1)h (left) to the hexagonal peak at (1,1)h (right) for temperatures decreasing from $T=1200$ K. The path traversed through reciprocal space is shown inset.

tion), and two occurred for temperatures increasing from $T=300$ K. The latter cycles immediately followed one of the cycles for decreasing temperatures. During each, the temperature was lowered or raised monotonically in steps of about 100 K, allowing about 30–60 min for stabilization. Typical temperature drifts during data acquisition were less than about $\Delta T=10$ K. As in the preceding subsection, all the transverse and longitudinal scans were fitted to Lorentzian line shapes for the purpose of extracting reliable peak amplitudes, positions, and widths. These were then used to generate the data shown in Figs. 10–15.

A sequence of low-resolution scans taken along the line joining the $(0,1)h$ hexagonal peak on the left to the $(1,1)h$ near-hexagonal peak on the right is shown in Fig. 7. The data were obtained for temperatures decreasing from $T=1200$ K and are plotted on a logarithmic scale. Perhaps the most striking feature of the data is the complete absence of any observable peak in the scan at $T=1200$ K. Evidently, at this temperature the hexagonal symmetry is completely lost. It is crucial to note that similar behavior was also observed in longitudinal scans through the $(1,0)h$ peak at these same temperatures. [The temperature dependence of the integrated intensity of the $(1,0)h$ peak is shown in Fig. 11.] In these scans, however, the substrate peak at $(1, 1, 0.07)c$ persisted above 1200 K, although very considerably weakened. On this basis, we conclude that above $T=1170$ K the top layer shares the (1×1) symmetry characteristic of the bulk. We suggest furthermore that the top, and possibly succeeding layers, are disordered above $T=1170$ K. Additional evidence supporting the latter is given in Ref. 1. Referring to Fig. 7, the hexagonal peaks at $(0,1)h$ and $(1,1)h$ and their first harmonics become visible when the temperature has been lowered to $T=1124$ K. At this temperature, the surface layer exists in the distorted-hexagonal phase. No higher harmonics are observed in the longitudinal scans until about $T=980$ K (near the rotational transition), where second- and, possibly, third-order harmonics first appear above the background. No additional harmonics appeared at any lower temperature.

High-resolution scans of the transverse line shapes (ω scans) of the hexagonal peak at $(1,0)h$ are plotted on a logarithmic scale in Fig. 8. These data were obtained for one cycle of the temperature, decreasing from about $T=1200$ to 762 K. Solid lines are the best fits obtained with Lorentzian line shapes. As mentioned above, no intensity was observed at the hexagonal $(1,0)h$ position until the temperature fell below about $T=1170$ K, and the surface layer was in the distorted-hexagonal phase. A typical scan taken at $T=1065$ K is shown in the top of the figure. All of the intensity at this temperature (which extends above the background nearly 3 orders of magnitude) is aligned with the [110] direction ($\omega=0$). As the temperature is lowered through $T=1000$ K, the first signs of additional scattering appear near $\omega=-0.81°$. Decreasing the temperature to $T=930$ K, both rotated components become visible at $\omega=\pm0.81°$, and the intensity grows as the temperature is decreased still further. Correspondingly, the intensity of the unrotated component decreases with decreasing temperature, and its

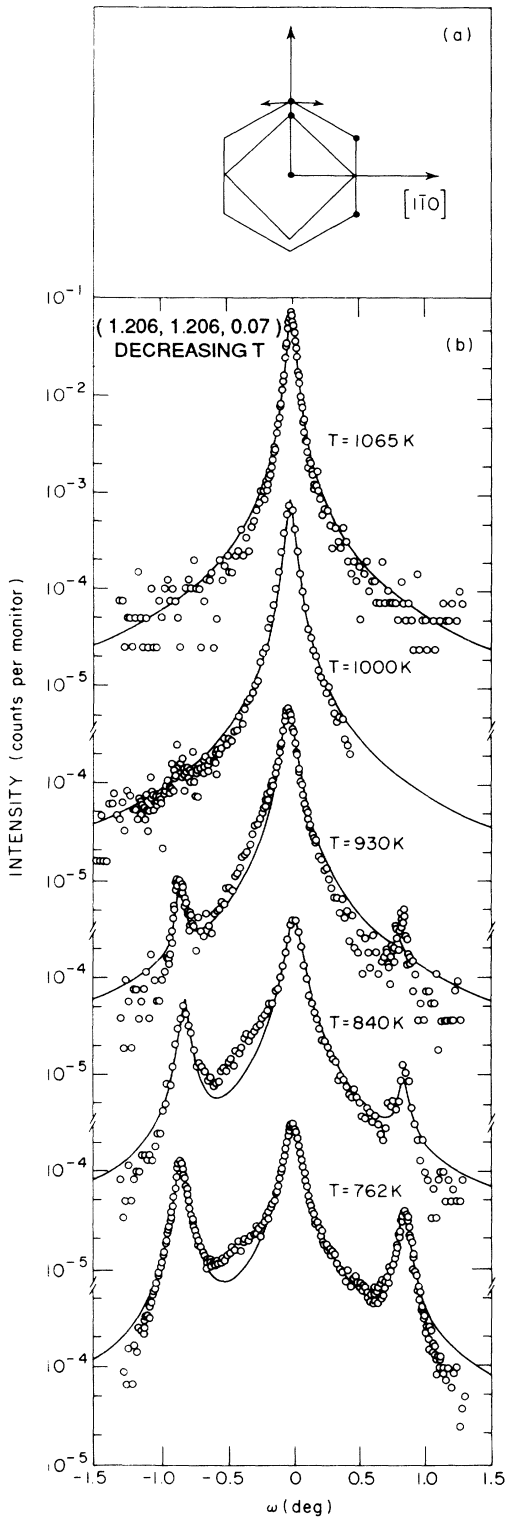

FIG. 8. Transverse scans through the hexagonal peak at $(1,0)h$ for temperatures decreasing from $T=1065$ to 762 K. The path traversed through reciprocal space is shown inset. Solid lines are the result of fits to Lorentzian line shapes.

width increases. The deviations of the data from simple Lorentzian behavior are asymmetric for positive and negative ω, and become more pronounced at lower temperatures. By $T=650$ K (see Fig. 5), the peak intensities of the rotated and unrotated components are similar.

The results of transverse scans through the hexagonal peak at $(1,0)h$ for temperatures increasing from $T=300$ K (and taken immediately after the data shown in Fig. 8) are shown in Fig. 9. The line shapes of the transverse scans obtained for increasing temperatures clearly do not reproduce the line shapes obtained for temperatures decreasing from $T=1200$ K. The width of the unrotated peak broadens further for increasing temperatures and the deviations from simple Lorentzian behavior increase. Despite the observation of hysteresis, by $T=965$ K (near the onset of the rotational transition for decreasing temperatures) the scattering at $\omega=\pm 0.81°$ has disappeared. Thus, in spite of the hysteresis, it is clear that the rotational transition is reversible.

On the basis of this, and similar data, we have deduced the existence of the three structural phases shown in Fig. 1. In the following, we quantify the temperature dependence of the parameters characterizing the longitudinal and transverse line shapes for all of the data obtained in the six cycles of the temperature, increasing and decreasing.

The integrated intensities of the rotated and unrotated components of the hexagonal peak at $(1,0)h$ and of their sum are plotted in Figs. 10 and 11, respectively. An abrupt increase in intensity for temperatures decreasing from $T=1200$ K is seen clearly. The width of transition, determined by observation of the intensity on the ratemeter (and not by performing detailed scans), is about 10 K. Below $T=1000$ K, the sum of the intensities of the rotated and unrotated components is approximately constant, to within the experimental errors (Fig. 11). The observed decrease in intensity of the unrotated component for decreasing temperatures is evidently approximately compensated in the sum by the increase in intensity of the rotated components (Fig. 10). The scatter in the data below $T=1000$ K prevents a reliable estimate of temperature dependence of the surface Debye-Waller factor. The surface Debye-Waller factor for the Au(001) surface was instead determined by reflectivity methods, and is given in Ref. 1.

Also shown in Fig. 11 is the temperature dependence of the intensity of the substrate peak at $(1, 1, 0.07)c$. In contrast to the hexagonal peak, the integrated intensity of the substrate peak decreases approximately linearly with increasing temperature until about $T=1170$ K, where it abruptly decreases by at least a factor of 100. Although considerably weaker, this peak nevertheless remains visible in the diffraction pattern above $T=1170$ K. No data above $T=1170$ K are shown in the figure because it was necessary to remove the analyzing crystal to find the peak at these temperatures, thereby preventing quantitative intensity comparison. The reduction in intensity of the substrate peak suggests that second and succeeding layers may also disorder as the temperature is increased above $T=1170$ K. These kinds of effects have been discussed for Pb(110) (Refs. 17 and 33) surfaces, and are elaborated

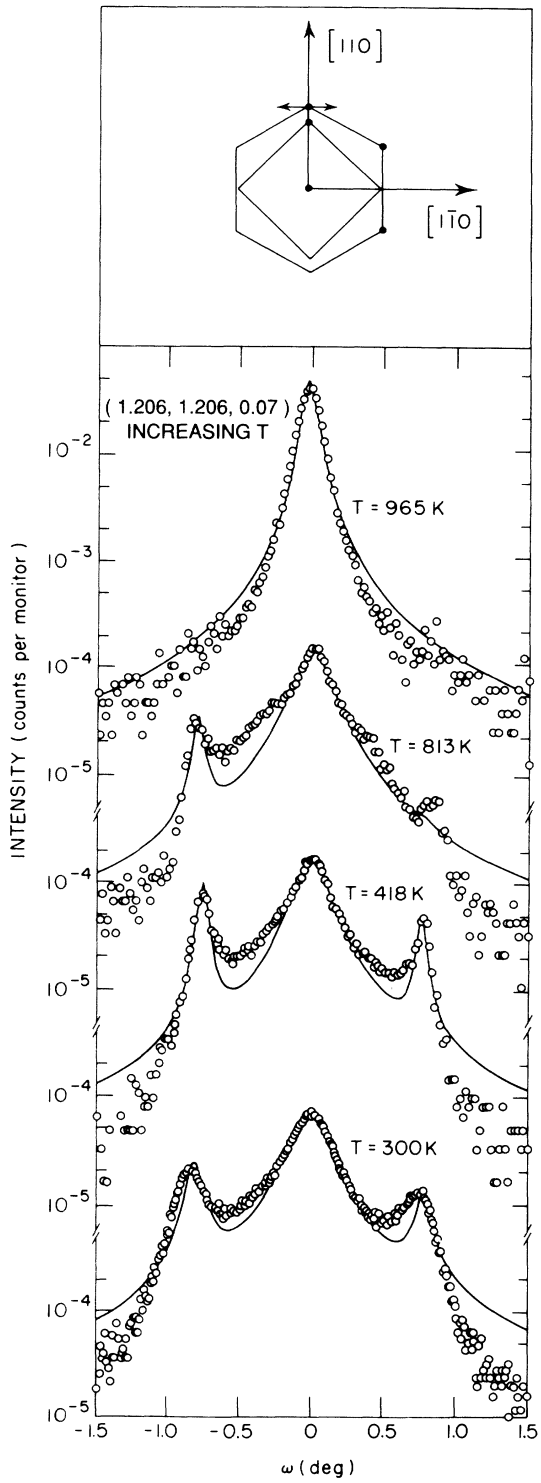

FIG. 9. Transverse scans through the hexagonal peak at $(1,0)h$ for temperatures increasing from $T=300$ to 965 K. The path traversed though reciprocal space is shown inset. Solid lines are the result of fits to Lorentzian line shapes. The line shapes for increasing temperatures are noticeably different from those for decreasing temperatures.

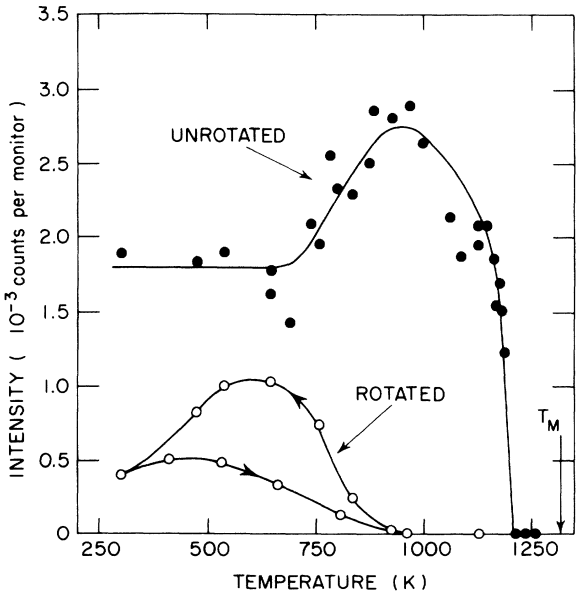

FIG. 10. Integrated intensities of the rotated and unrotated components of the hexagonal peak at (1,0)h plotted vs temperature. In both cases, the integrated intensities were computed from the amplitudes determined by Lorentzian fits, as discussed in the text. The arrows indicate hysteresis present in the temperature dependence of the rotated component. T_M indicates the position of the bulk melting temperature for bulk gold.

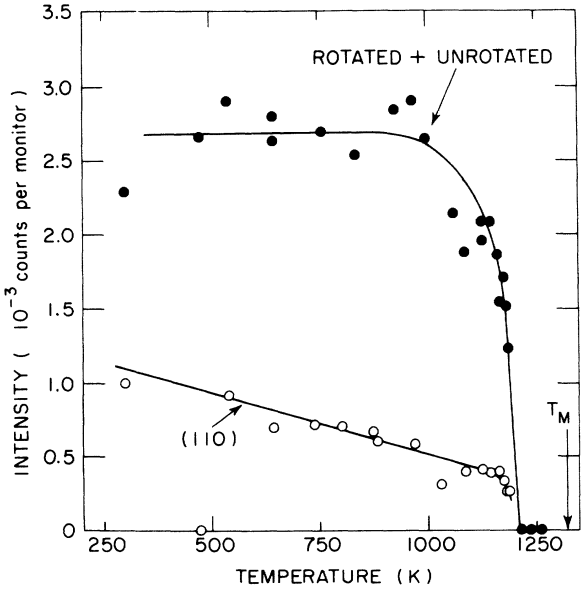

FIG. 11. Solid circles: the sum of the integrated intensities of the rotated and unrotated components of the hexagonal peak at (1,0)h for decreasing temperature. Open circles: the integrated intensity of the substrate peak at (1, 1, 0.07)c vs temperature. In both cases, the integrated intensities were calculated from the Lorentzian fits to the peaks amplitudes.

for Au(001) in Ref. 1.

The temperature dependence of the rocking widths (FWHM) of the transverse scans for the unrotated and rotated components of the hexagonal peak at (1,0)h is plotted in Fig. 12. Identical behavior was also obtained for the rocking-curve widths of the peaks at (0,1)h, which is not shown. As mentioned, these scans reflect the angular distribution of the rotated domains across the surface. At higher temperatures, in the distorted-hexagonal phase, the rocking widths of the peaks at (1,0)h and (1, 1, 0.07)c are constant, and equal to 0.05° and 0.03°, respectively. These widths are broader than the widths of the bulk (0,0,2) and (1,3,1) reflections, which are about 0.01°, or smaller. At $T=970$ K, near the rotational transition, the unrotated peak broadens; its width increases approximately linearly for decreasing temperatures to about 0.2° at $T=300$ K. The discontinuous change in the rotation angle from $\omega=0°$ to $\omega=0, \pm 0.81°$, is, therefore, accompanied by a continuous, broadening of the aligned peak. In contrast, the width of the substrate peak increases only slightly with decreasing temperatures. To within our statistics, the rocking widths of the rotated peaks are constant.

For temperatures increasing from $T=300$ K, the rocking width of the unrotated peak continues to broaden until about $T=600$ K. Above this temperature, the rocking width then decreases, until at the rotational transition near $T=970$ K, it reproduces its high-temperature value.

The temperature dependence of the transverse width above is to be compared with the temperature dependence of the longitudinal width, which is plotted in Fig. 13. The reciprocal of the longitudinal width of the unrotated component reflects the length scale over which hexagonal in-plane structural order exists. A full width of

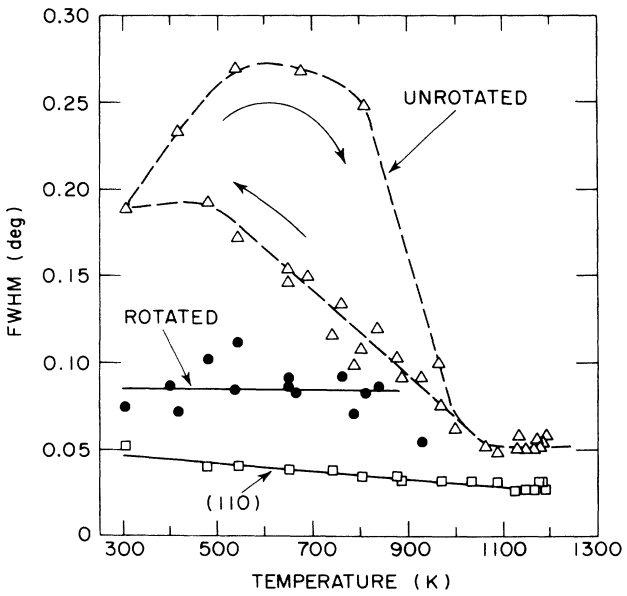

FIG. 12. Temperature dependence of the rocking-curve widths (FWHM) of the rotated and unrotated components of the hexagonal peak at (1,0)h, and of the substrate peak at (1, 1, 0.07)c. These were determined from Lorentzian fits as discussed in the text. The arrows indicate the hysteresis present for increasing and decreasing temperatures.

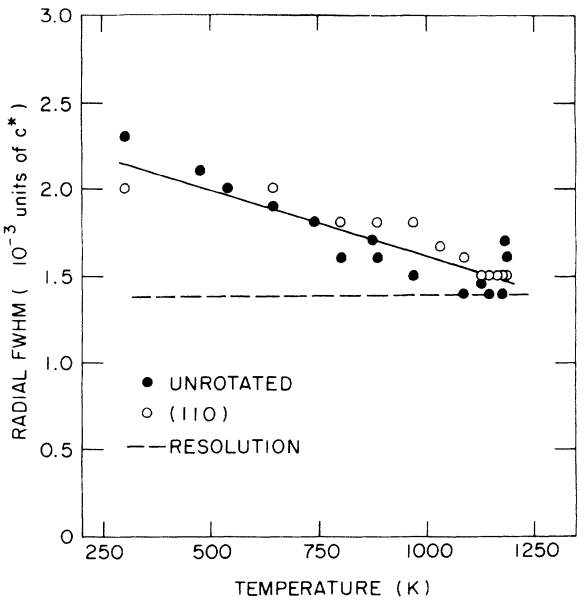

FIG. 13. Temperature dependence of the longitudinal widths (FWHM) of the unrotated component of the hexagonal peak at (1,0)h and of the substrate peak at (1, 1, 0.07)c. The dashed line indicates the instrumental resolution for this configuration.

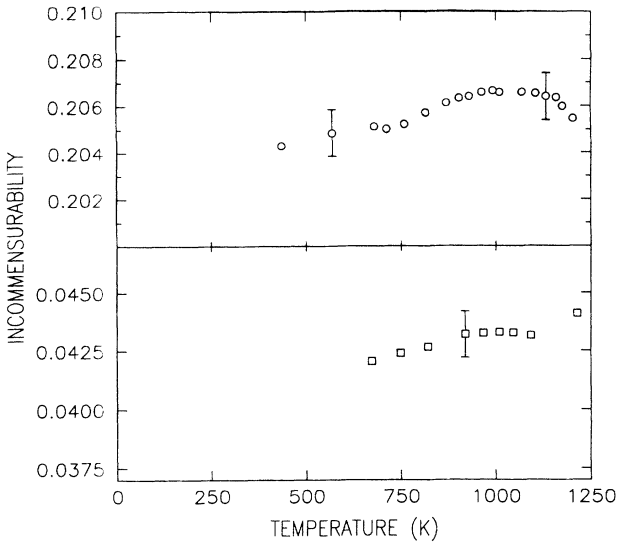

FIG. 14. Upper: temperature dependence of the incommensurability of the hexagonal peak at (1,0)h. Lower: temperature dependence of the incommensurability of the hexagonal peak at (1,2)h. These data were obtained using a Ge(111) analyzing crystal. The error, ± 0.001, is also indicated.

$0.0015c^*$ corresponds to a correlation length of several thousand angstroms, or larger. In the figure, the full width at half maximum of the hexagonal peak (solid circles) is resolution-limited (FWHM of $0.0015c^*$) in the distorted-hexagonal phase, but increases linearly with decreasing temperatures. Thus, the longitudinal and transverse widths are narrowest when the unit cell is most perfectly aligned to the [110] direction. These widths are maintained constant in spite of the fact that the integrated intensity of the hexagonal peak decreases by a factor of 2 near $T=1170$ K (Fig. 11). Similar behavior is mirrored in the temperature dependence of the longitudinal width of the substrate peak at (1, 1, 0.07)c. No hysteresis was discerned in the temperature dependence of the radial widths of either the hexagonal or substrate peaks. In addition, we observed no diffuse scattering from a well-correlated fluid phase which would be associated with a continuous (second-order) phase transition. The observed behavior is consistent, then, with a first-order transition at which the extent of disordered regions across the surface grows with increasing temperature. Unfortunately, instrumental temperature fluctuations were large enough to defeat detailed measurements very close to $T=1170$ K.

The incommensurability of the hexagonal overlayer along the [110] and [1$\bar{1}$0] directions is plotted versus temperature in Fig. 14. At each temperature, the positions of the hexagonal peaks at (1,0)h and (1,2)h and of the substrate peaks at (1, 1, 0.07)c and (2, 2, 0.07)c were measured (see Fig. 1). The incommensurability along the [110] direction was then calculated as

$$|(1,0)h-(1,1,0.07)c|/|(1,1,0.07)c|$$

and along the [1$\bar{1}$0] direction as

$$|(1,2)h-(2,2,0.07)c|/|(2,2,0.07)c| .$$

As may be seen in the figure, the results for the incommensurability in both directions appear to decrease slightly with decreasing temperature. It should be noted, however, that this variation spans the uncertainty of the measurement, and so may not be regarded as established. The average values of the incommensurability along the [110] and [1$\bar{1}$0] directions are 0.206 ± 0.001 and 0.043 ± 0.001, respectively. These values were used to calculate the average hexagonal lattice constants a and b reported in Sec. III A. Similarly, the rotation angle corresponding to the discontinuous transition of the hexagonal overlayer at $T=970$ K is shown plotted versus temperature in Fig. 15. To within the available statistics, it is approximately constant with an average value of $\pm0.81\pm0.05°$.

It is interesting to add here that at a later point in these experiments, the sample heater unexpectedly shorted to ground, while the sample was in the high-temperature, disordered phase. This caused a rapid quench to $T=800$ K, whereupon the temperature control was recovered. Under these conditions, transverse scans through the (1,0)h, (0,1)h, and, indeed all the overlayer peaks, revealed not only the peaks observed previously at $\omega=0$, $\pm0.81°$, but also additional peaks at $\omega=\pm0.3°$ (see Fig. 16). Upon subsequent heating and slower cooling, transverse line shapes as in Figs. 5, 6, and 8 were recovered. The small deviations from Lorentzian behavior shown in the transverse scans of Figs. 8 and 9 also suggest the possible existence of rotated hexagonal domains with rotation angles different from $\omega=0$, $\pm0.81°$.

From the data, it is clear that the most perfectly or-

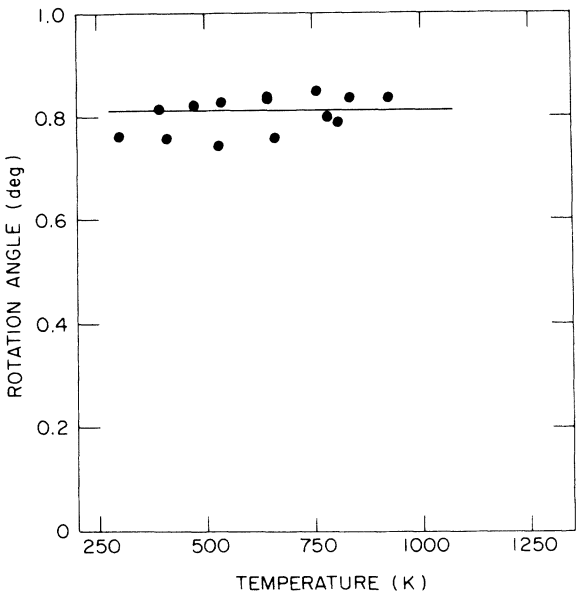

FIG. 15. Temperature dependence of the rotation angle for the hexagonal peak at (1,0)h in degrees. This angle was determined from the Lorentzian fits, as discussed in the text. The solid line gives the average value, $\omega = 0.81°$.

dered structure which exists on the Au(100) surface occurs in the distorted-hexagonal phase. In this phase, the longitudinal width is resolution-limited, which suggests that the correlation length for hexagonal in-plane order is at least several thousand angstroms in size. Similarly, the transverse width takes its smallest value in this phase. Perhaps not coincidentally, the higher harmonics of the hexagonal peaks are also not observed in the distorted-hexagonal phase, consistent with a reduced in-plane distortion. It is not until there is a discontinuous change in rotational angle, from $\omega = 0°$ to $\omega = \pm 0.81°$, that the most dramatic evolution in line shape with temperature begins. Below $T = 970$ K, both the transverse and longitudinal linewidths increase, and higher harmonics of the hexagonal structure become visible. In addition, the line shapes of the hexagonal peaks display hysteresis, and appear to depend on the rate of cooling. It therefore seems clear that rotated, hexagonal domains form on the surface of Au(100) at the expense of the long-range order present in the distorted-hexagonal phase. Such effects are a hallmark of incommensurate systems near commensurability (see, for example, Refs. 12 and 13), and, in general, even continuous rotational transitions may display a large hysteresis.[12–14] In the present case, the existence of metastable states with rotation angles differing from $\omega = 0°, \pm 0.81°$ (Fig. 16) could make the achievement of equilibrium particularly difficult.

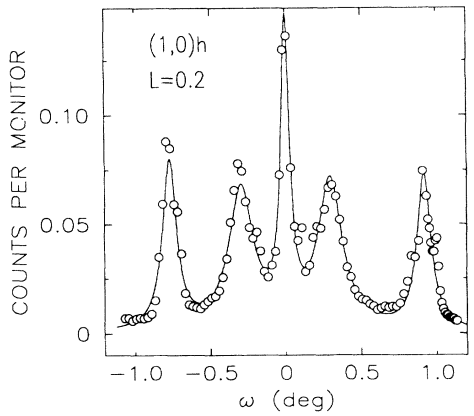

FIG. 16. Transverse scan of (1,0)h obtained after a rapid quench from $T = 1200$ to 800 K.

D. Orientational epitaxy

The possibility that an incommensurate overlayer residing on a single-crystal substrate may be rotated away from a high-symmetry direction was originally predicted by Novaco and McTague[34] and subsequently observed, for a monolayer of Ar adsorbed on graphite, by LEED.[35] Since then, an extensive body of literature, concerned with orientational epitaxy, commensurate-incommensurate transitions, and melting in two-dimensional systems, has accumulated. All of the rare gases adsorbed on graphite substrates have been studied by a variety of different techniques. Excellent summary articles of three recent x-ray studies have been published by Specht *et al.*,[14] by D'Amico *et al.*,[13] and by Hong *et al.*[12] We note that rotational effects have also been observed for alkali-metal[36,37] adsorbates on various transition-metal substrates and for Pb adsorbates electrochemically deposited on Ag and Au.[38] Current theories[34,39,40] (which, however, ignore the effect of finite-temperature fluctuations, neglect any substrate response, and are principally carried out for triangular overlayers and triangular substrates assumed at equilibrium) present the following scenario. For overlayers very close to commensurability, the rotation angle is zero. At a critical incommensurability, which depends on the overlayer elastic constants and the substrate potential, there is an onset of rotation. There can be either a jump in the rotation angle or a continuous increase from zero depending on the overlayer elastic constants.[39,40] With further increase in the incommensurability, the rotation angle increases continuously, finally becoming linearly proportional to the incommensurability. Behavior consistent with this has been observed in a number of instances.[13,14,35,36] However, the rotational transition observed here does not obviously fit into this scheme. Instead, we observe both a discontinuous change in rotational angle and a broadening of the unrotated peak without a corresponding change in the incommensurability. On the other hand, a very similar transition has been observed (among others) in the case of Xe on graphite,[12] where at high temperatures the Xe overlayer jumps from a nonrotated phase to a rotated phase ($\omega = \pm 0.6°$) with essentially no accompanying change in incommensurability. If we calculate the ratio of the rotation angle to the misfit for the Au(001) surface, we find (0.014 rad)/0.206 = 0.068. The corresponding quantity for Xe adsorbed on graphite is 0.22,[12,13] while for Ar adsorbates it is 0.55.[13,33] The applicability of current (equilibrium)

theories of orientational epitaxy to the rotational transition observed on the Au(001) surface remains to be established.

IV. CONCLUSIONS

Using synchrotron x-ray-scattering techniques, we have identified three distinct structural phases exhibited by the Au(001) surface between $T=300$ K and the bulk melting transition at $T=1337$ K. They are (1) disordered ($1170<T<1337$ K), (2) distorted-hexagonal ($970<T<1170$ K), and (3) rotated, distorted-hexagonal ($300<T<970$ K). In the high-temperature phase, the x-ray-diffraction pattern has the (1×1) symmetry of the bulk, consistent with a disordered surface. Below $T=1170$ K, there is a reversible transition to an incommensurate, two-dimensional structure of hexagonal symmetry, but which is significantly modulated by the substrate. Below $T=970$ K, there is a reversible transition to a rotated, incommensurate, hexagonal structure. Both the incommensurability and the average rotational angle are weakly temperature dependent. Yet, in the rotated, distorted-hexagonal phase the line shapes of the hexagonal diffraction peaks show hysteresis, and the length scale over which there exists in-plane order is reduced. The remarkable behavior exhibited by an elemental metal surface remains a challenge to our present understanding of two-dimensional physics.

ACKNOWLEDGMENTS

We have benefited from conversations with D. Abernathy, J. D. Axe, R. J. Birgeneau, K. L. D'Amico, G. Grübel, G. Held, I. K. Robinson, and A. Sandy. Helpful conversations with J. D. Axe, J. Bohr, K. L. D'Amico, P. Fuoss, D. E. Moncton, J. F. Fuhrman, A. Meade, K. M. Mohanty, A. Roberts, I. K. Robinson, and W. Shoenig during the design and construction of the UHV surface apparatus described in the text are also gratefully acknowledged. We would particularly like to thank G. Ownby for his assistance during the experiment. Work performed at Brookhaven National Laboratory is supported by the U.S. Department of Energy (DOE) under Contract No. DE-AC0276CH00016. Work performed at the Massachusetts Institute of Technology was supported by the U.S. National Science Foundation under Grant No. DMR-87-19217 (Materials Research Laboratory Program) and under Grant No. DMR-88-06591 (Solid State Physics Program). Work performed at Oak Ridge National Laboratory is sponsored by the Division of Materials Sciences, U.S. DOE, under Contract No. DE-AC02-84OR21400, with Martin Marietta Energy Systems.

[1]B. M. Ocko, D. Gibbs, K. G. Huang, D. M. Zehner, and S. G. J. Mochrie (unpublished).

[2]M. A. Van Hove, R. J. Koestner, P. C. Stair, J. B. Biberian, L. L. Kesmodel, I. Bartos, and G. A. Somorjai, Surf. Sci. **103**, 189 (1981).

[3]P. W. Palmberg and T. N. Rhodin, Phys. Rev. **161**, 586 (1967).

[4]D. M. Zehner, B. R. Appleton, T. S. Noggle, J. W. Miller, J. H. Barret, L. H. Jenkins, and E. Schow III, J. Vac. Sci. Technol. **12**, 454 (1975).

[5]D. G. Fedak and N. A. Gjostein, Phys. Rev. Lett. **16**, 171 (1966).

[6]G. E. Rhead, J. Phys. F **3**, L53 (1973).

[7]G. Binnig, H. Rohrer, Ch. Gerber, and E. Stoff, Surf. Sci. **144**, 321 (1984).

[8]K. H. Reider, T. Engel, R. H. Swendsen, and M. Manninen, Surf. Sci. **127**, 223 (1983).

[9]F. Ercolessi, E. Tosatti, and M. Parrinello, Phys. Rev. Lett. **57**, 719 (1986); Surf. Sci. **177**, 314 (1987); F. Ercolessi, A. Bartolini, M. Garofalo, M. Parrinello, and F. Tosatti, Phys. Scr. **T19**, 399 (1987); B. W. Dodson, Phys. Rev. B **35**, 880 (1987).

[10]K. Yamazaki, K. Takayanagi, Y. Tanishiro, and K. Yagi, Surf. Sci. **199**, 595 (1988).

[11]D. Gibbs, B. M. Ocko, D. M. Zehner, and S. G. J. Mochrie, Phys. Rev. B **38**, 7303 (1988).

[12]H. Hong, C. J. Peters, A. Mak, R. J. Birgeneau, P. M. Horn, and H. Suematsu, Phys. Rev. B **40**, 4797 (1989).

[13]K. L. D'Amico, D. E. Moncton, E. D. Specht, R. J. Birgeneau, S. E. Nagler, and P. M. Horn, Phys. Rev. Lett. **53**, 2250 (1984); K. L. D'Amico, J. Bohr, D. E. Moncton, and D. Gibbs, Phys. Rev. B **41**, 4368 (1990).

[14]E. D. Specht, A. Mak, C. Peters, M. Sutton, R. J. Birgeneau, K. L. D'Amico, D. E. Moncton, S. E. Nagler, and P. M. Horn, Z. Phys. B **69**, 347 (1987).

[15]I. K. Robinson, Phys. Rev. Lett. **50**, 1145 (1983).

[16]G. A. Held, J. L. Jordan-Sweet, P. M. Horn, A. Mak, and R. J. Birgeneau Phys. Rev. Lett. **59**, 2075 (1987).

[17]P. Fuoss, L. Norton, and S. Brennan, Phys. Rev. Lett. **60**, 2046 (1988).

[18]I. K. Robinson, E. H. Conrad, and D. S. Reed, J. Phys. (Paris) (to be published).

[19]S. G. J. Mochrie, Phys. Rev. Lett. **59**, 304 (1987).

[20]B. M. Ocko and S. G. J. Mochrie, Phys. Rev. B **38**, 7378 (1988).

[21]J. W. Chung, K. Evans-Lutterodt, E. D. Specht, R. J. Birgeneau, P. J. Estrup, and A. R. Kortan, Phys. Rev. Lett. **59**, 2192 (1987); I. K. Robinson, A. A. MacDowell, M. S. Altman, P. J. Estrup, K. Evans-Lutterodt, J. D. Brock, and R. J. Birgeneau, *ibid.* **62**, 1275 (1989).

[22]K. G. Huang, A. Sandy, S. G. J. Mochrie, D. Gibbs, and D. M. Zehner (unpublished).

[23]R. Feidenhans'l, Surf. Sci. Rep. **10**, 105 (1989).

[24]I. K. Robinson, Phys. Rev. B **33**, 3830 (1986).

[25]S. G. J. Mochrie, D. M. Zehner, B. M. Ocko, and D. Gibbs, Phys. Rev. Lett. **64**, 2925 (1990).

[26]*NSLS Handbook* (Brookhaven National Laboratory, Upton, NY, 1990).

[27]Franke and Heydrich Corp., D7080 Aalen, West Germany.

[28]P. Fuoss and I. K. Robinson, Nucl. Instrum. Methods **222**, 171 (1984).

[29]Electrofusion Corp., Fremont, CA 94555.

[30]R. Pynn, J. D. Axe, and R. Thomas, Phys. Rev. B **13**, 2965 (1975).

[31]R. Cowley, Adv. Phys. **29**, 1 (1980).
[32]A. Erbil, A. R. Kortan, R. J. Birgeneau, and M. S. Dresselhaus, Phys. Rev. B **28**, 6319 (1983).
[33]A. B. Pluis, A. W. Denier van der Gon, J. W. M. Franken, and J. F. van der Veen, Phys. Rev. Lett. **59**, 2678 (1987).
[34]A. D. Novaco and J. P. McTague, Phys. Rev. Lett. **38**, 1286 (1977); J. P. McTague and A. D. Novaco, Phys. Rev. B **19**, 5299 (1979).
[35]C. G. Shaw, S. C. Fain, Jr., and M. D. Chinn, Phys. Rev. Lett. **41**, 955 (1978); S. C. Fain, M. D. Chinn, and R. D. Diehl, Phys. Rev. B **21**, 4170 (1980).
[36]T. Aruga, H. Tochihara, and Y. Murata, Phys. Rev. Lett. **52**, 1794 (1984), and references therein.
[37]D. Doering and S. Semancik, Phys. Rev. Lett. **53**, 66 (1984).
[38]M. G. Samant, M. F. Toney, G. L. Borges, L. Blum, and D. M. Melvoy, J. Phys. Chem. **92**, 220 (1988).
[39]J. Villain, Phys. Rev. Lett. **41**, 36 (1978).
[40]H. Shiba, J. Phys. Soc. Jpn. **46**, 1852 (1979); **48**, 211 (1980).

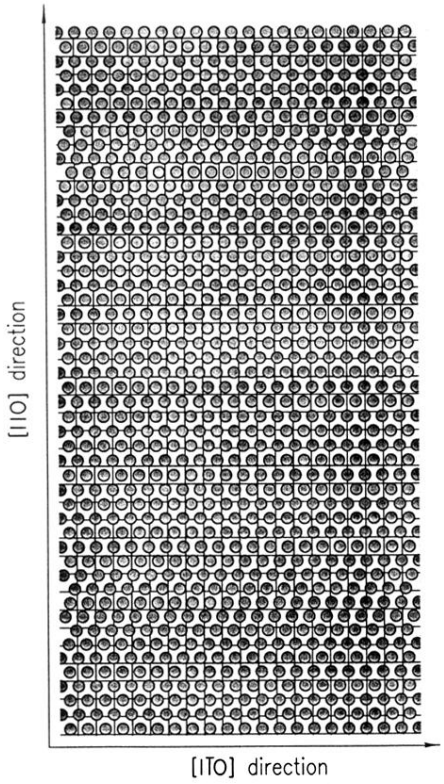

FIG. 4. Ball model of possible incommensurate domain walls running parallel to the [1$\bar{1}$0] direction, and separating locally commensurate regions. The $\hat{\mathbf{z}}$-component of the displacement field (corrugation) is not shown.